

KLEIN TUNNELING IN THE PRESENCE OF RANDOM IMPURITIES

S. PALPACELLI

*Numidia s.r.l., via Giacomo Peroni
130, 00131 Roma, Italy
silviapalpacelli@gmail.com*

M. MENDOZA* and H. J. HERRMANN†

*ETH Zürich, Computational Physics for Engineering Materials
Institute for Building Materials, Schafmattstrasse 6
HIF, CH-8093 Zürich, Switzerland
*mmendoza@ethz.ch
†hjherrmann@ethz.ch*

S. SUCCI

*Istituto per le Applicazioni del Calcolo C.N.R.
Via dei Taurini, 19, 00185, Roma, Italy
and
Freiburg Institute for Advanced Studies, Albertstrasse
19, D-79104 Freiburg, Germany
succi@iac.cnr.it*

Received 7 August 2012

Accepted 31 August 2012

Published 19 November 2012

In this paper, we study Klein tunneling in random media. To this purpose, we simulate the propagation of a relativistic Gaussian wave packet through a disordered medium with randomly distributed potential barriers (impurities). The simulations, based on a relativistic quantum lattice Boltzmann (QLB) method, permit to compute the transmission coefficient across the sample, thereby providing an estimate for the conductivity (or permeability) as a function of impurity concentration and strength of the potentials. It is found that the conductivity loss due to impurities is significantly higher for wave packets of massive particles, as compared to massless ones. A general expression for the loss of conductivity as a function of the impurity percentage is presented and successfully compared with the Kozeny–Carman law for disordered media in classical fluid-dynamics.

Keywords: Klein paradox; disorder media; quantum lattice Boltzmann.

PACS Nos.: 66.35.+a, 03.65.Pm, 72.80.Vp.

1. Introduction

As opposed to classical quantum mechanics, where fermions tunneling into a barrier are exponentially damped, relativistic scattering was shown by Klein in 1929¹ to follow a very unexpected behavior: If the potential is of the order of the fermion mass or higher, the barrier becomes virtually transparent to the fermions. The capability of quantum wave functions to undergo zero reflection from a potential barrier much higher than the energy of the wave function itself is a property that relies exclusively upon the spinorial nature of the Dirac wave function. It stands in stark contrast with the corresponding nonrelativistic behavior, which predicts an exponential decay of the transmission coefficient with the difference $V_0 - E$, V_0 being the height of the barrier and E the wave function energy. Based on an analytical solution of the scattering problem for a monochromatic plane wave, it has been shown that, depending on a series of geometrical and energy parameters, special angles of incidence (resonant angles) provide literally zero reflectivity^{2,3}: the plane wave goes completely across the barrier. Furthermore, in the presence of a random media, transport laws similar to the ones ruling fluid motion in diluted porous media, may be expected to apply. We refer here, e.g. to the Carman–Kozeny law,^{4–8} which relates the permeability of a porous medium (conductivity of the medium) to the solid concentration (impurity density).

The conductivity of two-dimensional massless fermions in disordered media has become the object of intense studies in the literature.^{9–13} The Klein–paradox (KP) has also been addressed in the recent literature,^{13–20} but mostly in connection with plane wave formulations. Some works have also considered localized Gaussian wave packets,^{21,22} but only in connection with single and multiple ordered barriers. The contribution of the present work to this subject encompasses the three following directions: (i) Investigate the KP for the case of Gaussian wave packets, rather than plane waves, for *disordered* samples; (ii) Discuss the viability of semi-classical descriptions of fermionic excitations in disordered media, based on quantitative analogies with flows in porous media; (iii) Expose the QLB method as a new computational tool for fermionic transport in disordered media, which might bear a special interest for prospective implementations on parallel computers.

We wish to remark that while Klein tunneling leads to spectacular effects for plane waves across one-dimensional barriers, its import for the case of two-dimensional random media might turn out to be relatively milder, for two reasons. First, because in confined nonperiodic geometries and the presence of impurities,²³ plane waves might be hard to realize, hence the motivation for inspecting localized wave functions, such as prototypical Gaussian wave packets. However, since Gaussian wave packets, or any other localized wave function, necessarily include nonresonant frequencies, which suffer partial reflection, they are expected to experience less spectacular KP effects than plane waves. Second, whenever the wave packet extent exceeds the impurity size, it can split and turn around the obstacle like a classical fluid, thereby undergoing partial transmission, with no need for any quantum

tunneling through the barrier. Based on the above, it appears of interest to explore to what extent Klein tunneling is indeed affecting fermionic transport within generic disordered media.

The paper is organized as follows: first, we introduce a brief description of the QLB method²⁴; second, we study the case of Klein tunneling of a Gaussian wave packet through a rectangular potential barrier. Subsequently, we present numerical solutions of the Dirac equation in the presence of random impurities, thereby providing an estimate for the effects of the impurity concentration on the conductivity of the medium, for both cases, massless and massive Dirac fermions. The simulations are performed using a QLB model, which is also introduced as a new tool to study transport phenomena through disordered media. Finally, we discuss and summarize the results.

2. The Quantum Lattice Boltzmann Method

The QLB method²⁴ is a quantum-kinetic technique originally devised to solve non-relativistic single-body Schrödinger equation and other related quantum problems, such as the Gross–Pitaevski equation for Bose–Einstein condensates.²⁵ Only recently, it has been shown to provide a second-order accurate solver for relativistic wave scattering and propagation.²⁶ To forestall any confusion, we wish to clarify that QLB is targeted to (genuine or effective) one-body quantum wave functions, and it does not refer to the dynamics of statistical ensembles, such as those described by the quantum Boltzmann equation. The name Boltzmann is attached to QLB simply as an inheritance from its classical counterpart, the lattice Boltzmann method, which is indeed a minimal form of Boltzmann kinetic equation to solve classical fluid-dynamic problems from a statistical mechanics (kinetic theory) perspective.³⁹ Since the method is relatively new in the relativistic context, for the sake of self-containedness, we revisit here its main technical aspects. For full details, see Refs. 27 and 28.

QLB equation was initially derived from a formal parallel between the kinetic lattice Boltzmann equation and the single-particle Dirac equation.^{24,29,a} For our purpose, it proves expedient to transform the standard form of the Dirac equation into the Majorana form, in which all matrices are real,³⁰

$$[\partial_t + c(-\alpha^x \partial_x + \beta \partial_y - \alpha^z \partial_z) + i\omega_c \alpha^y - igI]\psi = 0. \quad (1)$$

This form is obtained by multiplying the standard Dirac equation on the left- and right-hand side by the involution matrix $U = 2^{-1/2}(\alpha^y + \beta)$. In the above, c is the light speed, I is the identity operator and $\omega_c = mc^2/\hbar$ is the Compton frequency for a particle of mass m , with \hbar the reduced Planck's constant. The wave function ψ is a

^aWe wish to forestall any potential confusion, possibly arising from the denomination “Boltzmann” in the QLB framework. Here “Boltzmann” stems from the formal analogy between the *single-particle* Dirac equation and the Boltzmann equation of classical statistical mechanics. In this respect, QLB should be kept distinct from the quantum Boltzmann equation, typically used to address collective quantum transport phenomena.

complex four-spinors and α and β are the standard Dirac matrices. The last term couples the wave function to an applied scalar potential $V(x, y, z)$ via the coefficient $g = qV/\hbar$, where q is the electric charge.³⁰ Note that since the spin states mix-up during propagation (spinning particles), there is no basis in which all three matrices $\alpha^x, \alpha^y, \alpha^z$ can be simultaneously diagonalized.

Let us consider a one-dimensional version of the Dirac equation. In particular, let Z be a unitary matrix, diagonalizing the streaming matrix $-\alpha^z$:

$$Z = \frac{1}{\sqrt{2}} \begin{pmatrix} 0 & -1 & 0 & 1 \\ 1 & 0 & -1 & 0 \\ 0 & 1 & 0 & 1 \\ 1 & 0 & 1 & 0 \end{pmatrix}. \quad (2)$$

Applying the matrix Z to Eq. (1), the streaming matrix along z is diagonalized and the collision matrix is also transformed accordingly

$$[\partial_t + cZ^{-1}(-\alpha^z)Z\partial_z + Z^{-1}(-c\alpha^x\partial_x + c\beta\partial_y + i\omega_c\alpha^y - igI)Z]Z^{-1}\psi = 0. \quad (3)$$

Neglecting any dependence of ψ on the x and y coordinates, Eq. (3) may be written as a pair of one-dimensional Dirac equations

$$\begin{aligned} \partial_t u_{1,2} + c\partial_z u_{1,2} &= \omega_c d_{2,1} + igu_{1,2}, \\ \partial_t d_{1,2} - c\partial_z d_{1,2} &= -\omega_c u_{2,1} + igd_{1,2}, \end{aligned} \quad (4)$$

for the variables (u_1, d_2) and (u_2, d_1) that represent the rotated wave function $Z^{-1}\psi = (u_1, u_2, d_1, d_2)^T$. The components u and d propagate up and down the z axis, respectively, and the subscripts indicate the spin up (1) and spin down (2) states, respectively. The system of Eq. (4) may be treated as a Boltzmann equation for a pair of complex distribution functions $u_{1,2}$ and $d_{1,2}$.²⁴ Equation (4) may thus be discretized using the same approach as in lattice Boltzmann method, i.e. by integrating along the characteristic light-cones $dz = \pm cdt$.

The resulting system of algebraic equations reads as follows:

$$\begin{aligned} \hat{u}_{1,2} - u_{1,2} &= \frac{1}{2} \tilde{m}(d_{2,1} + \hat{d}_{2,1}) + \frac{1}{2} i\tilde{g}(u_{1,2} + \hat{u}_{1,2}), \\ \hat{d}_{1,2} - d_{1,2} &= -\frac{1}{2} \tilde{m}(u_{2,1} + \hat{u}_{2,1}) + \frac{1}{2} i\tilde{g}(d_{1,2} + \hat{d}_{1,2}), \end{aligned} \quad (5)$$

where the hat superscript ($\hat{\cdot}$) indicates that the wave function is evaluated at the end-point of the corresponding streaming step, namely

$$\begin{aligned} \hat{u}_{1,2} &= u_{1,2}(z + \Delta z, t + \Delta t), & u_{1,2} &= u_{1,2}(z, t), \\ \hat{d}_{1,2} &= d_{1,2}(z - \Delta z, t + \Delta t), & d_{1,2} &= d_{1,2}(z, t). \end{aligned} \quad (6)$$

The dimensionless Compton frequency is $\tilde{m} = \omega_c \Delta t$ and the dimensionless scalar potential is $\tilde{g} = g(z, t) \Delta t$.

The pair of Eqs. (5) can be solved algebraically, delivering explicit expressions for $\hat{u}_{1,2}$ and $\hat{d}_{1,2}$:

$$\begin{aligned}\hat{u}_{1,2} &= au_{1,2} + bd_{2,1}, \\ \hat{d}_{1,2} &= ad_{1,2} - bu_{2,1},\end{aligned}\tag{7}$$

where the coefficients a and b are

$$a = \frac{1 - \Omega/4}{1 + \Omega/4 - i\tilde{g}}, \quad b = \frac{\tilde{m}}{1 + \Omega/4 - i\tilde{g}}, \quad \Omega = \tilde{m}^2 - \tilde{g}^2.$$

These coefficients satisfy $|a|^2 + |b|^2 = 1$, so that the right-hand side of Eq. (7) corresponds to multiplying the rotated wave function $Z^{-1}\psi = (u_1, u_2, d_1, d_2)^T$ by the **unitary collision matrix**

$$Q = \begin{pmatrix} a & 0 & 0 & b \\ 0 & a & b & 0 \\ 0 & -b & a & 0 \\ -b & 0 & 0 & a \end{pmatrix}.\tag{8}$$

The streaming step propagates $u_{1,2}$ upwards and $d_{1,2}$ downwards, along the light-cones given by $\Delta z = \pm c\Delta t$. Note that this unitary operation is numerically *exact*, without round-off error, because the distribution function is integrally transferred from the source to the destination site, and no fractional transport is involved. Since both streaming and collisions step are unitary, the overall QLB scheme evolves the discrete wave function through a sequence of unitary operations for any value of the discrete time step Δt . In addition, since streaming proceeds upwind only (no centered spatial differences) along the discrete light-cones associated with each component Ψ_i , the QLB dispersion relation is automatically free from fermion-doubling.³¹

This, together with the excellent efficiency of the method,^b especially on parallel computers,^{32,33} makes QLB an appealing candidate for computational studies of fermionic transport through disordered media.

The scheme extends to multiple dimensions through an operator splitting technique. Within this method, the three-dimensional Dirac equation splits into the sum of three numbers of one-dimensional equations, each involving spatial derivatives along one single direction. Each of the three stages representing evolution by a time step dt is accomplished by rotating ψ to diagonalize the relevant streaming matrix, taking one time step of the existing one-dimensional QLB scheme described above, and rotating ψ back to its original basis. The algorithm is thus composed of the following three steps: (1) Rotate ψ with X^{-1} , collide with $X^{-1}\hat{Q}X$, stream along x , rotate back with X ; (2) Rotate ψ with Y^{-1} , collide with $Y^{-1}\hat{Q}Y$, stream along y ,

^bThe model updates about five million lattice sites per second on a standard PC (Intel Processor of 2.4 GHz)

rotate back with Y ; (3) Rotate ψ with Z^{-1} , collide with $Z^{-1}\hat{Q}Z$, stream along z , rotate back with Z . This form emphasizes the symmetry between the three steps, but since the streaming matrix along y is already diagonal in the Majorana form, $Y = I$ is the identity matrix. The matrix X reads as follows:

$$X = \frac{1}{\sqrt{2}} \begin{pmatrix} -1 & 0 & 1 & 0 \\ 0 & 1 & 0 & -1 \\ 1 & 0 & 1 & 0 \\ 0 & 1 & 0 & 1 \end{pmatrix} \quad (9)$$

and the Z matrix is given in Eq. (2) above.

The collision-term splits into three parts, each of which is combined with the corresponding streaming step. The collision matrix thus coincides, up to a unitary transformation, with the collision matrix for the one-dimensional QLB scheme, with a time step $1/3dt$.²⁸ In particular, \hat{Q} is given by:

$$\hat{Q} = \begin{pmatrix} \hat{a} & 0 & 0 & -\hat{b} \\ 0 & \hat{a} & \hat{b} & 0 \\ 0 & -\hat{b} & \hat{a} & 0 \\ \hat{b} & 0 & 0 & \hat{a} \end{pmatrix}, \quad (10)$$

where the coefficients

$$\hat{a} = \frac{1 - \Omega_3/4}{1 + \Omega_3/4 - i\tilde{g}_3}, \quad \hat{b} = \frac{\tilde{m}_3}{1 + \Omega_3/4 - i\tilde{g}_3},$$

are written in terms of the rescaled dimensionless Compton and potential frequencies

$$\Omega_3 = \tilde{m}_3^2 - \tilde{g}_3^2, \quad \tilde{m}_3 = \frac{1}{3}\omega_c dt, \quad \tilde{g}_3 = \frac{1}{3}g dt.$$

The pattern of + and – signs in the \hat{b} terms on the off-diagonal of \hat{Q} follows the same pattern as the α^y matrix. The rotated matrices $X^{-1}\hat{Q}X$ and $Z^{-1}\hat{Q}Z$ have the same sign pattern as Q , but \hat{Q} does not.

Summarizing, QLB provides a unitary, explicit algorithm for quantum wave functions in which information propagates along classical trajectories represented by a sequence of three one-dimensional light-cones, thereby avoiding any mixing of the spinorial components during the streaming step. Although detailed comparisons with other techniques remain to be developed, there are reasons to believe that such simplification may result in enhanced computational efficiency, especially with parallel computers in mind. **Finally, we wish to point out that the same algorithm describes both relativistic and nonrelativistic quantum wave packets, depending on the value of the mass m and the characteristic strength of the potential energy.**

3. Relativistic Gaussian Wave Packets

Our simulations will be performed in two spatial dimensions, (for more details see Ref. 28). The propagation of a plane wave through a rectangular potential barrier was discussed in Ref. 34. However due to the fact that it only applies to monochromatic plane waves, i.e. infinitely extended states which may not necessarily be realized under all experimental conditions, it is of interest to explore to what extent are such results affected by the finite extent of the wave function. KP effects using Gaussian wave packets have been addressed in recent numerical studies.^{21,22,35,36}

Here, we build a semi-analytical approach and test it against numerical simulations.^c

For simplicity, we consider a Gaussian wave packet of the form:

$$\psi_l(x, y) = \frac{A_l}{(4\pi\sigma^2)^{1/2}} e^{-r^2/4\sigma^2} e^{i(k_x x + k_y y)}, \quad l = 1, 2, \quad (11)$$

where $r^2 = x^2 + y^2$, $A_1 = 1/A$, $A_2 = e^{i\phi}/A$ with $A = \sqrt{A_1^2 + A_2^2}$ and ϕ is the angle of the momentum vector. The rectangular box potential of height V_0 and width D is defined as follows:

$$V(x) = \begin{cases} V_0, & \text{if } 0 < x < D, \\ 0, & \text{elsewhere.} \end{cases} \quad (12)$$

Given the linearity of the Dirac equation and the fact that wave packets are constituted by a Gaussian superposition of plane waves, it is natural to express the transmission coefficient of a Gaussian wave packet of size σ through the following convolution:

$$T_\sigma(k_x, k_y) = \int_{S_f} G\left(\frac{\mathbf{k} - \mathbf{k}'}{\sigma_k}\right) T(k'_x, k'_y) dk'_x dk'_y, \quad (13)$$

where $S_f = \pi k_F^2$, with $k_F^2 = k_x^2 + k_y^2$, denotes the Fermi area and G is a Gaussian kernel of width $\sigma_k = 1/\sigma$ in momentum space. The function $T(k_x, k_y)$ is the transmission coefficient of a plane wave with vector $\mathbf{k} \equiv (k_x, k_y)$, which according to Ref. 34, can be calculated as $T = 1 - |r|^2$ with

$$r = \frac{2ie^{i\phi}(ss')^{-1} \sin(q_x D)(\sin\phi - ss' \sin\theta)}{[e^{-iq_x D} \cos(\phi + \theta) + e^{iq_x D} \cos(\phi - \theta)] - 2i \sin(q_x D)}, \quad (14)$$

where ϕ is the incidence angle, $q_x^2 = (E - V_0)^2/\hbar^2 c^2$, $\theta = \tan^{-1}(k_y/q_x)$ is the refraction angle, $s = \text{sign}(E)$, $s' = \text{sign}(E - V_0)$ and E is the energy.

Since the transmission coefficient for a plane wave only depends on the wave number k_y , and due to the fact that the x component of the wave vector experiences a perfect transmission, as a first-order *approximation*, we perform the convolution in

^cWe have also tested our QLB scheme against the numerical results given in Ref. 22, and found satisfactory agreement.

just one dimension, k_y , i.e.

$$T_\sigma(k) = \int_{-k_F}^{k_F} G\left(\frac{k - k'}{\sigma_k}\right) T(k') dk', \quad (15)$$

where we have defined $k \equiv k_y$. By setting $k' = k + q$, and expanding $T(k + q)$ around $q = 0$ to second-order, Eq. (15) delivers

$$T_\sigma(k) \sim T(k) + \frac{\sigma_k^2}{2} T''(k) + O(\sigma_k^2), \quad (16)$$

where T'' is the second derivative of T with respect to k . The above expression means that resonant peaks ($T'(k_r) = 0, T''(k_r) < 0$) are smoothed out whenever the filter width σ_k is sufficiently high, or, more precisely, $\sigma_k^2 > |T''(k)|/2T(k)$. This smoothing is the effect of nonresonant wave numbers. Given that $\sigma = 1/\sigma_k$, one could readily estimate the minimal width σ above which the secondary resonant peak would no longer be seen by the Gaussian wave packet. However, the asymptotic expansion given by Eq. (16) fails to represent the actual transmission coefficient of the Gaussian wave packet near the secondary resonant peak, the reason being that, around that peak, a second-order expansion is grossly inaccurate because $\sigma^2 T'' \sim 1$ and higher orders will be even less accurate. As a result, the convolution integral, Eq. (15), needs to be computed.

3.1. Computing the convolution

To gain a quantitative sense of the dependence of the transmission coefficient of the Gaussian wave packet with the spatial spread σ , we have numerically computed the convolution integral of Eq. (15), for the following values $\sigma/D = 0.15, 0.31, 0.46, 0.92, 1.85$, where $D = 100$ nm is the width of the potential barrier. The parameters are the same as in Ref. 34, namely $E = 0.08$ eV, $V_0 = 0.2$ eV and $D = 100$ nm. The results are shown in Fig. 1. From this figure, it is seen that, for $\phi = 0$, $T(k_r) = T(k_F \cos(\phi_r))$ goes from 1 to 0.7348, slightly over a 25% reduction. The same figure also shows that around the secondary resonance (at $\phi = 2\pi/9$), narrow wave packets with $\sigma/D < 0.46$ feature $T \sim 0.5$, with no sign of the secondary resonant peak. On the other hand, the secondary peak is seen to re-emerge for $\sigma/D > 0.92$, i.e. when σ is of the order of 100 nm, comparable with the barrier width. With $\sigma/D = 1.85$, the secondary peak is recovered, but only to about 80%. Note that, for $\phi = \pi/2$, the transmission coefficient is not zero, which is a consequence of the approximation made to obtain Eq. (15) from Eq. (13). However, as shown in Sec. 3.2, the numerical simulation of the transmission coefficient using QLB, shows generally a pretty satisfactory agreement with the approximation of Eq. (15).

In order to use the plane wave approximation, one needs to ensure that the condition $\sigma > D$ is fulfilled, which sounds pretty plausible. However, this condition is

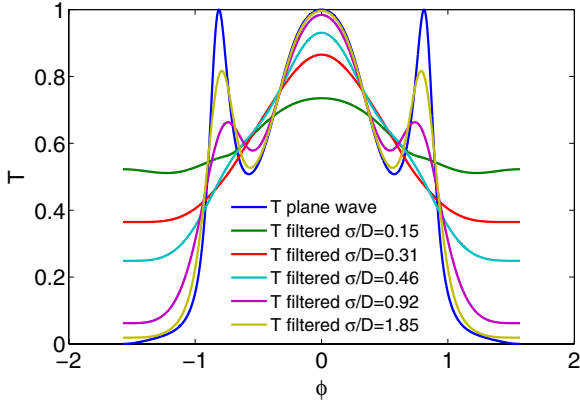


Fig. 1. (Color online) The transmission coefficient of a Gaussian wave packet, as computed with the analytical convolution, Eq. (15), as a function of the incidence angle ϕ for $\sigma/D = 0.15, 0.31, 0.46, 0.92, 1.85$. The blue line corresponds to the unfiltered case, $\sigma \rightarrow \infty$, corresponding to a plane wave.

strongly dependent on the angle of incidence. In particular, it is far more stringent for oblique than for head-on ($\phi = 0$) incidence. Indeed, for $\phi = 0$, $\sigma/D \sim 0.5$ yields a substantial $T = 0.9$ for $\phi = 0$, while at $\phi = 2\pi/9$, we obtain a mere $T \sim 0.4$. At $\sigma/D \sim 2$, perfect transmission, $T = 1$, is practically recovered at $\phi = 0$, while for $\phi = 2\pi/9$, $T \sim 0.8$, i.e. about 80% of full transmission.

We conclude that, for head-on incidence ($\phi \sim 0$), the transmission coefficient of Gaussian packets is still similar to the one of plane waves, as soon their extent becomes comparable to the barrier width. On the other hand, the secondary resonance, at oblique incidence, is highly affected by the finite-size of the wave packet, and full recovery of perfect transmission seems to require wave packet extents significantly larger than the barrier width.

3.2. Numerical simulations

The analytical expression of Eq. (15) has been compared against direct numerical simulation of the Dirac equation, using the QLB method. In order to back-up the previous findings, we have computed full numerical solutions of the Dirac equation using a QLB solver. The simulations are performed on 1024^2 , 2048^2 and 4096^2 grids, depending on the size of the Gaussian packet.

The physical parameters are taken from Ref. 34, i.e. $E = 0.080$ eV, $V_0 = 0.200$ eV and $D = 100$ nm.

Space and time units are defined by the lattice spacing in space and time, Δx and $\Delta t = \Delta x/c$, respectively, whereas the energy unit is taken as $\Delta E = \hbar/\Delta t$. The lattice spacing is chosen in such a way to resolve well the barrier width, in our case $\tilde{D} = D/\Delta x = 52$, corresponding to $\Delta x \sim 1.92$ nm. This gives $\Delta t = \Delta x/c \sim 1.92 \times 10^{-15}$ s and $\Delta E \sim 0.35$ eV. The following sequence of wave packets spreading, $\sigma = 24, 48, 96$

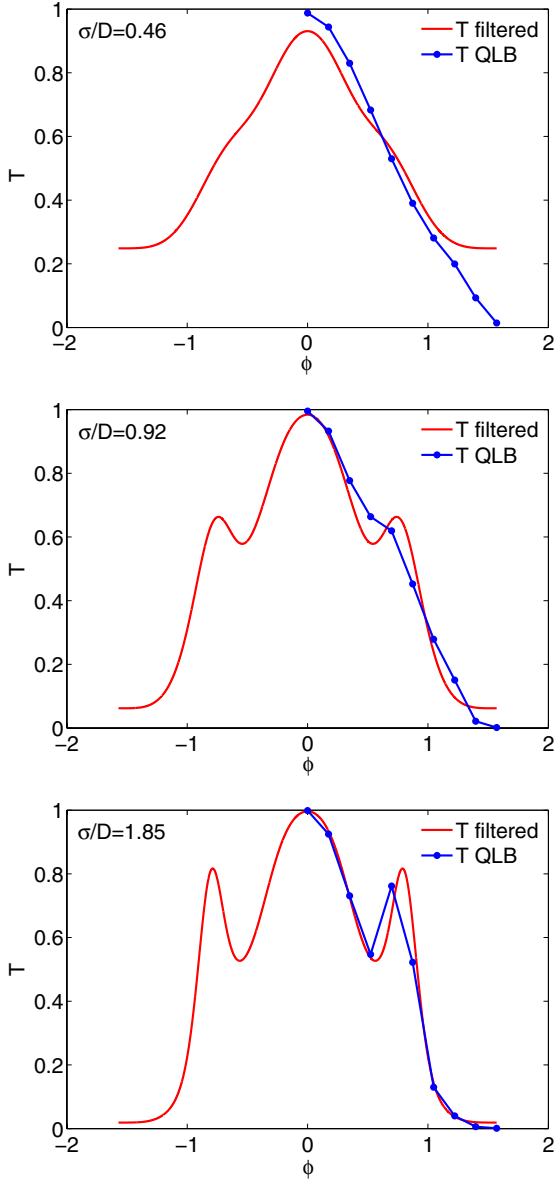


Fig. 2. (Color online) The transmission coefficient of a Gaussian wave packet as a function of the incidence angle ϕ for $\sigma = 24, 48$ and 96 (in lattice units), corresponding to $\sigma/D = 0.46, 0.92, 1.85$, as computed via convolution (solid line) and by QLB simulations (line with dots).

has been simulated, with $D = 52$, all in lattice units. The results of the QLB simulations appear substantially in line with the prediction of the convolution integral, i.e. they clearly show the disappearance of the secondary peak for $\sigma/D < 0.46$, and its progressive reappearance above this threshold (see Fig. 2). Note that, different

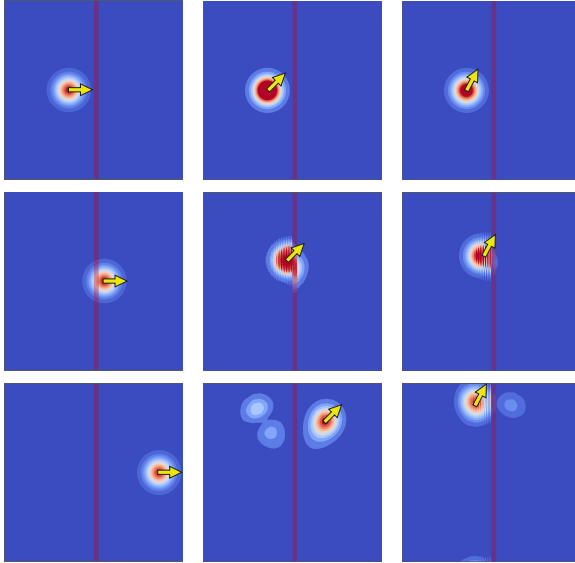


Fig. 3. (Color online) Snapshots of the wave packet density at various instants, $t = 0, 420, 1050$ (lattice units), for the case $\phi = 0$ (left) and $\phi = 2\pi/9$ (middle) and $\phi = \pi/3$ (right) for $\sigma/D = 1.85$. In the middle, as one can see, after significant distortion in the intermediate stage of the evolution, the wave packet manages to be transmitted across the barrier to a substantial extent ($T = 0.76$). On the other hand, at the right, the packet is mostly bounced-back by the barrier, with transmission coefficient as low as $T = 0.13$. For visualization purposes, the color bar scale has been modified independently for each figure.

from the solution of the convolution integral, Eq. (15), the transmission coefficient measured by the simulation is zero for $\phi = \pi/2$, as should be expected, but the appearance of the second resonant peak is still retained.

In Fig. 3, we show typical snapshots of the wave packets for the cases $\phi = 0, 2\pi/9$ and $\pi/3$, for $\sigma/D = 1.85$. The snapshots clearly show that, in the case $\phi = 0$, the wave packet crosses the barrier totally unperturbed, with literally no distortion at any stage of the evolution. In the case of oblique resonant propagation, the packet still manages to cross the barrier to a large extent, ($T = 0.76$), with significant distortions in the intermediate stages of the evolution, leaving 24% of the packet behind. Finally, in the case of oblique nonresonant propagation, $\phi = \pi/3$, the packet is mostly bounced-back by the barrier, with a transmission coefficient as low as $T = 0.13$.

4. Klein–Paradox in Random Media

To gain insight into the macroscopic properties of a medium affected by the presence of impurities, it is of interest to investigate the propagation of relativistic wave packets within a disordered sample. To analyze these transport phenomena, we simulate the propagation of a relativistic Gaussian wave packet through a two-dimensional domain composed of three regions: an inlet region, where the wave



Fig. 4. (Color online) Sketch of the domain setting used in our simulations of the propagation of a Gaussian wave packet through a porous medium.

packet is positioned at the initial time $t = 0$; the impurity region, i.e. the central part of the domain where randomly distributed barriers (impurities) are located; and the outlet region, which is the final region, where measurements of the transmitted wave packets are taken. Since Klein tunneling is a single-particle effect, in the sequel we shall neglect any fermion–fermion interaction and consider the interaction of a single wave packet with a random distribution of impurities. Given that the wave packet loses momentum on the impurities, the permeability (conductivity) of the sample can be defined and measured, in close analogy with a classical fluid through porous media.^d

The impurity concentration is given by $C = Nd^2/A$, where N is the number of square impurities of cross-section d^2 , distributed over a total area $A = L_y \times L_z$. Here, L_y and L_z represent the vertical and horizontal lengths of the simulation zone, respectively. The impurities are randomly located, and have the same size, shape and potential value. For the present simulations, $d = 8$ and C is varied in the range 0.001–0.05. In Fig. 4, the computational domain is sketched, periodic boundary conditions are imposed at top and bottom boundaries, while a bounce-back condition is enforced at the inlet, and an open boundary condition is imposed at the outlet (so that the transmitted wave packet is not reflected back). This implies that the transmission coefficient will always converge to the unit value asymptotically in time.

We use a square lattice of size 2048×512 cells, such that the regions $[0, 512] \times 512$, $[512, 1536] \times 512$ and $[1536, 2048] \times 512$ correspond to the inlet, impurity and outlet regions, respectively. The lattice spacing is chosen in such a way as to properly resolve the smallest lengths in the problem, namely the obstacle diameter D , as well as the wave packet extent λ . The cell size is chosen to be $\Delta x = 0.96$ nm, corresponding to $\sigma = 48$ lattice spacings for the spreading of the initial Gaussian wave packet and $d = 8$ for the obstacle side. This yields an energy $E = 0.117$ (80 meV in physical units).

In our study, we use two values for the mass of the particles, $m = 0$ and $m = 0.1$ ($mc^2 = 0.1 \hbar/\Delta t \sim 0.07$ eV in physical units), and vary the impurity potential and the concentration. We note that the energy of the massive Gaussian wave packet is

^dWe have also performed simulations where massless and massive particles carry the same energy, and come to the very same conclusions: massive wave packets show smaller transmittivity than massless ones.

given by $E = \sqrt{k_0^2 + \sigma^{-2} + m^2}$ (in lattice units). Since throughout this study $k_0 \ll 1$ and $\sigma \gg 1$, the width contribution can be safely neglected, to obtain

$$E \sim \sqrt{k_0^2 + m^2}. \quad (17)$$

Since we are principally interested in the momentum losses against the impurities, in the sequel we shall consider the case where the massless and massive particles have the same momentum. Based on the expression (17), this means that the massive particle is a factor $\sqrt{1 + m^2/k_0^2}$ more energetic than the massless one.

Five barrier heights are considered, namely $V = 25, 50, 100, 200$ and 285 meV. Note that, while the first two lie below E , hence can be overcome classically, the others can only be traversed head-on via quantum tunneling. It should be further observed, though, that since the wave packet is wider than the single impurity, i.e. $\sigma > d$, even in the case $E < V$, the wave packet can split and turn around the obstacle like a “classical” fluid. Our results can be classified according to the energy of the particles, the potential of the barrier and their mass as follows: weak potentials, $V < E - mc^2$; intermediate potentials, $E - mc^2 < V < E + mc^2$; and strong potentials, $V > E + mc^2$. The transmission coefficient $T(t)$ is obtained by computing $T(t) = \int_{z>z_{\text{outlet}}} \rho(z, y, t) dz dy$, where ρ is the wave packet density defined as $\rho = |u_1|^2 + |u_2|^2 + |d_1|^2 + |d_2|^2$, with $\psi = (u_1, u_2, d_1, d_2)^T$ being the Dirac quadruplet introduced in Eq. (1). For the two-dimensional system discussed in this paper, the Dirac equation only involves two streaming matrices along z and y , respectively, so that we can set $\alpha^x = 0$. In the absence of magnetic field, the up-down components of the quadruplet collapse, and the Dirac equation for the resulting bispinor can be described in terms of 2×2 Pauli matrices.³⁷

4.1. Wave packet mass $m=0$

In this first set of simulations, we fix $m = 0$, and vary the impurity concentration, C and the strength of the impurity potential, V . In Fig. 5, we fix the value of V and we compare T while varying the impurity percentage, including the reference value for the pure sample $C = 0$. From this figure, we observe that the wave packet takes longer to regroup for high impurity concentration and high impurity potential. This is a natural consequence of the randomness induced in the wave function by the disordered media. However, in all cases, the complete wave packet is reconstructed after some time, with no stagnant regions left behind. This can be related to the momentum loss due to the presence of the impurities, and therefore the motion of the wave packet experiences a corresponding slow-down. Note that, in order to recover the complete wave function, the simulations have been performed in a longer domain. Otherwise the right-moving wave packet would leave the outlet region too early while the left-mover is still in the domain. In order to provide a measurement of momentum dissipation, i.e. the loss of conductivity due to impurities, we compute the momentum transmission

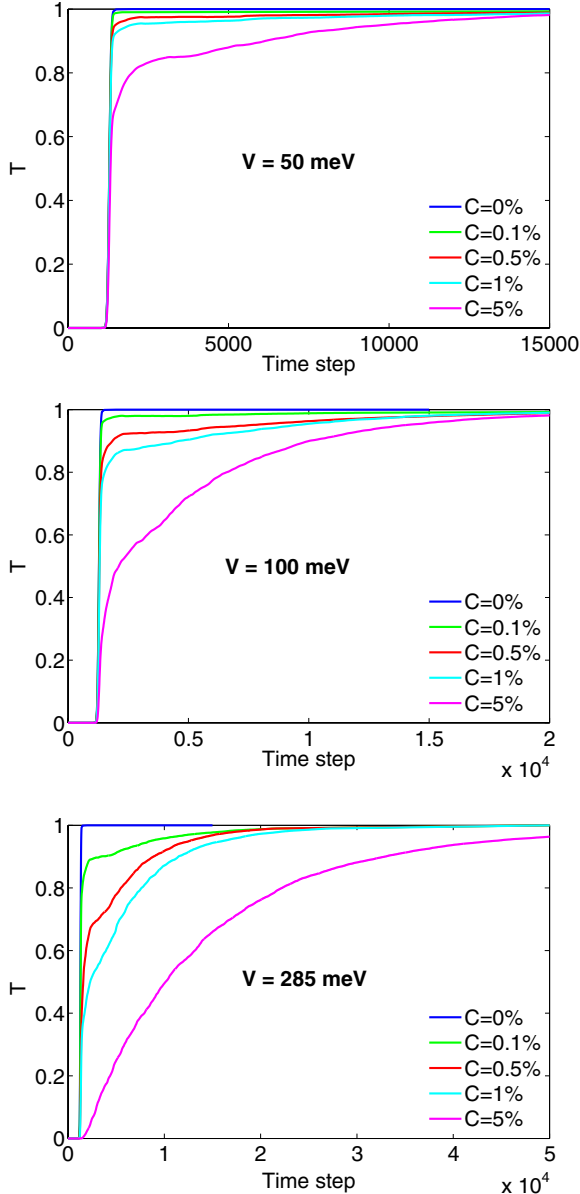


Fig. 5. (Color online) Transmission coefficient as a function of time for the impurity potential set at $V = 50, 100$ and 285 meV while varying the impurity percentage C ($C = 0.1, 0.5, 1$ and 5%) for $m = 0$.

coefficient as follows:

$$T_{Jz}(t) = \int_{z>z_{\text{out}}} J_z(z, y, t) dz dy, \quad (18)$$

where

$$J_z = \psi^\dagger A_z \psi + \psi^\dagger A_z^\dagger \psi, \quad (19)$$

is the z -component of the current density with A_z the streaming matrix along z and $\psi = (u_1, u_2, d_1, d_2)^T$ the Dirac quadrispinor.

In Fig. 6, we fix the value of V and compare T_{J_z} , while varying the impurity percentage. The subscript J_z denotes the transmission coefficient due to the z -component of the current density, J_z . As a reference, we also plot $T_{J_z}(t)$ when the impurity percentage is set to $C = 0$. From Fig. 6 we can observe that, unlike the density, the momentum transmission coefficient does not saturate at unity (its value in the inlet region at the beginning of the simulation), because momentum is irreversibly lost in the impurity region. Furthermore, as expected, the momentum loss increases with increasing impurity potential and concentration.

As a characteristic quantity associated with the dynamics of the transmission coefficient T , in Fig. 7, we report the escape time, $t_{0.9}$, i.e. the time at which the transmission coefficient reaches 90%, (i.e. at 90% of the wave packet is transmitted through the obstacle region). As above, we plot $t_{0.9}$ as a function of the impurity percentage for two values of V . We notice that for high impurity concentration the Gaussian wave packet takes longer to cross the impurity barrier. The same effect occurs when the impurity potential is increased. At low impurity concentration, $C = 0.001$, the effect of the potential barrier is relatively minor, but, as the concentration is increased, the escape time grows approximately linearly with the barrier voltage.

In Fig. 8, we show some representative snapshots of the first 1800 time steps of the simulation, for impurity percentage $C = 0.5\%$ and $V = 50$ meV. Here, we can see the way how the wave packet is scattered by the impurities, generating a plane front, as a result of the fragmentation of the wave function due to the random obstacles.

4.2. Wave packet mass $m = 0.1$

Next, we repeat the same simulations for the case of massive particles, with $m = 0.1$. Note that, since $mc^2/E = 0.83$, the rest energy is a significant fraction of the kinetic energy, and therefore the wave function comes in the form of a superposition of two wave packets, both moving at the speed of light, along opposite directions and mixing through the nonzero mass term.

In Fig. 9, we fix the value of V and compare T , while varying the impurity concentration C . As a reference, we also plot T with $C = 0$. From the results, we observe that the wave packet takes longer to cross the impurity region than for the case of $m = 0$ (the time it takes to reach a unit value of the transmission coefficient is longer). This is due to the slow-down of the wave function as compared to the speed of light, because of the nonzero particle mass. Note the peak in the transmission coefficient, once the wave packet exits from the impurity region. This is due to the fact that T_{J_z} takes negative values in the late stage of the evolution, indicating the

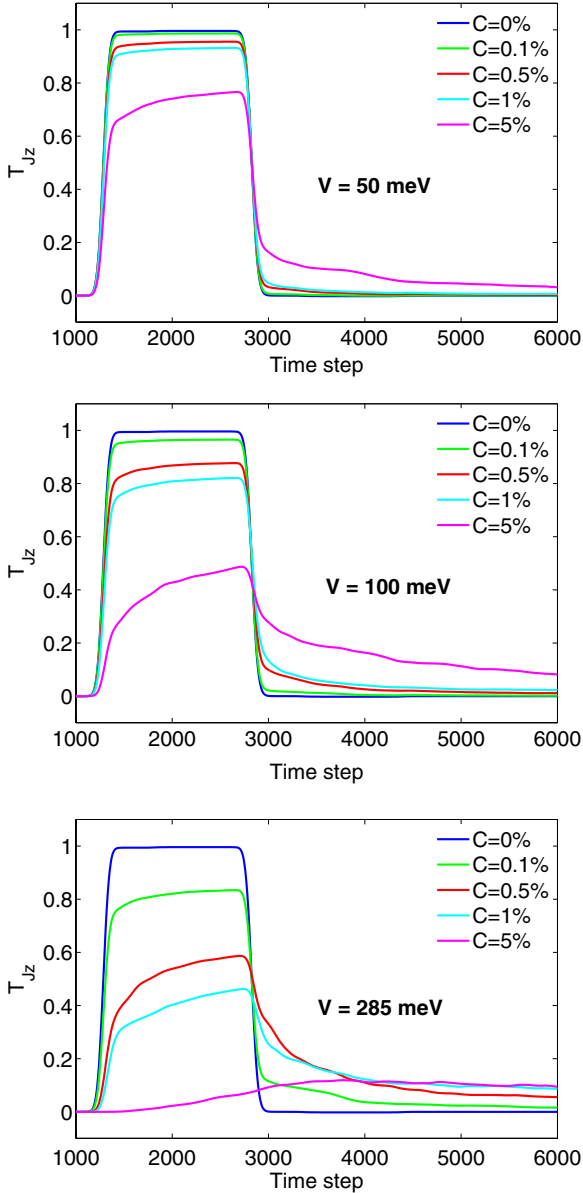


Fig. 6. (Color online) Momentum transmission coefficient T_{Jz} as a function of time for the impurity potential set at $V = 50, 100$ and 285 meV while varying the impurity percentage C ($C = 0.1, 0.5, 1$ and 5%) for $m = 0$.

prevalence of the left-moving component of the wave packet once the right-moving one has left the domain.

We compute the momentum transmission coefficient using Eqs. (18) and (19). In Fig. 10, we fix the value of V and compare T_{Jz} while varying the impurity

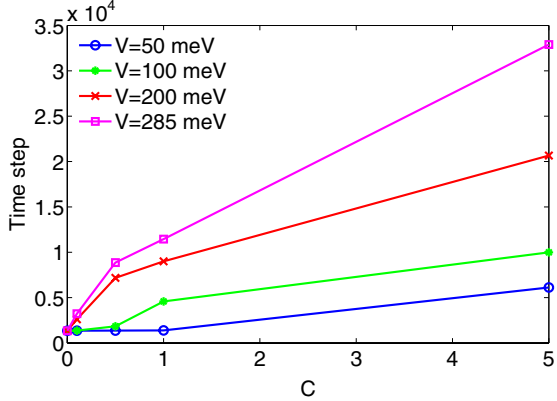


Fig. 7. (Color online) Time at which 90% of the wave packet has been transmitted, $t_{0.9}$, as a function of the impurity percentage for fixed values of V and $m = 0$. The potential barriers are as follows: $V = 50, 100, 200$ and 285 meV. The impurity percentage values are $C = 0.1\%, 0.5\%, 1\%$ and 5% .

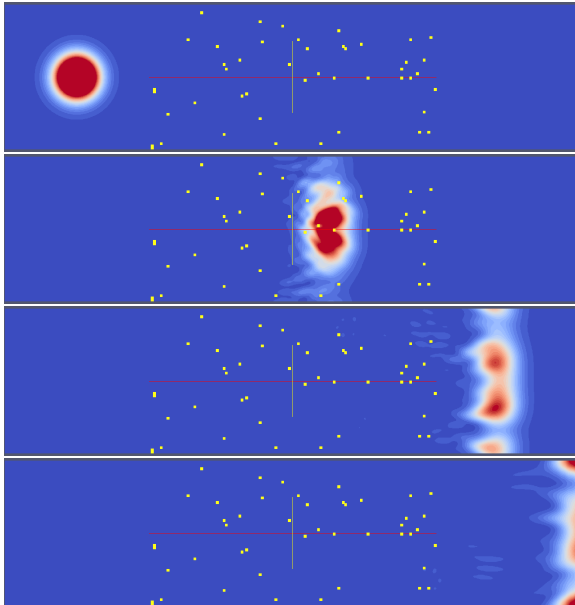


Fig. 8. (Color online) Wave packet density ρ at times = 0, 900, 1500 and 1800 (lattice units) for the simulation performed with impurity percentage $C = 0.5\%$ and $V = 50$ meV.

percentage. As a reference, we also plot $T_{Jz}(t)$ when the impurity percentage is set to zero. Note that, as expected, due to the inertia when the mass is increased, the curve of the momentum transmission becomes wider than for the case of zero mass, reflecting the fact that the wave packet takes longer to move across the impurity region. In addition, the maximum momentum is smaller than for the case of zero

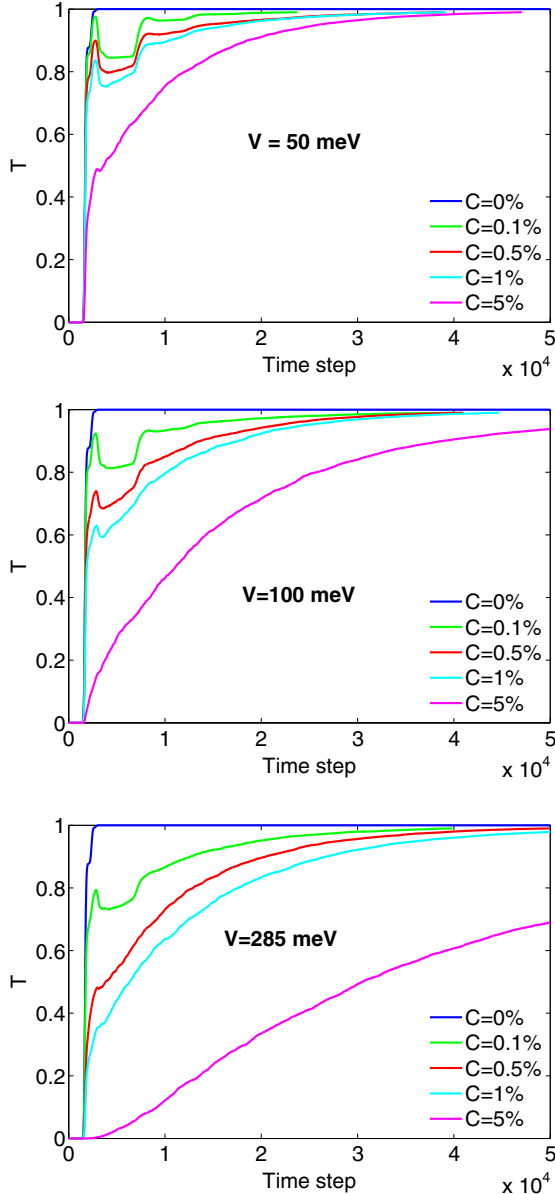


Fig. 9. (Color online) Transmission coefficient as a function of time for the impurity potential set at $V = 50, 100$ and 285 meV while varying the impurity percentage ($C = 0.1, 0.5, 1$ and 5%) for $m = 0.1$.

mass, which indicates higher momentum losses. Thus, a nonzero mass of the (quasi)-particles, results in higher momentum losses. Also to be noted, are the negative values of T_{J_z} in the late stage of the evolution, indicating the presence of a left-moving component, most likely due to a spurious reflection at the outlet boundary.

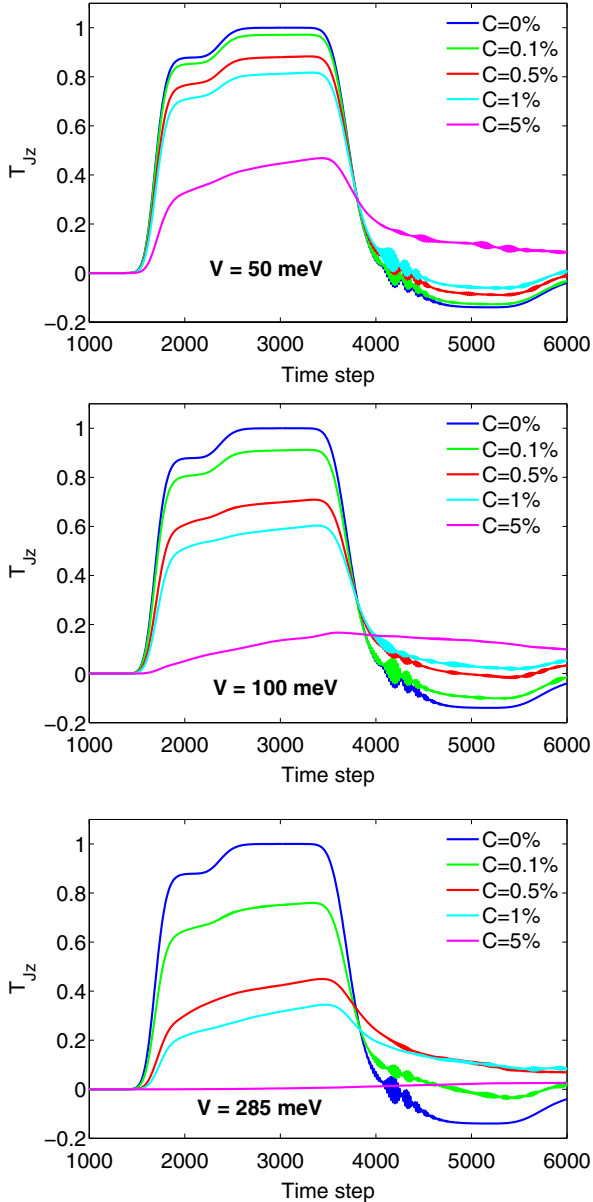


Fig. 10. (Color online) Momentum transmission coefficient T_{Jz} as a function of time for the impurity potential set at $V = 50, 100$ and 285 meV while varying the impurity percentage ($C = 0.1, 0.5, 1$ and 5%) for $m = 0.1$.

In Fig. 11, we show selected snapshots from the first 1800 time steps of the simulation for impurity percentage $C = 0.5\%$ and $V = 50 \text{ meV}$. From this figure, we observe that a portion of the wave packet gets “trapped,” moving at lower speed, within the impurity medium, while another portion manages to move out faster.

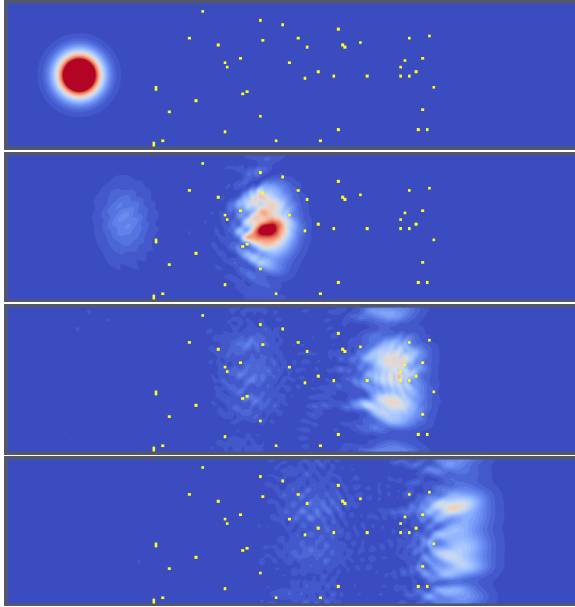


Fig. 11. (Color online) Wave packet density ρ at times 0, 900, 1500 and 1800 (lattice units) for the simulation performed with impurity percentage = 0.5% and $V = 50$ meV and with $m = 0.1$.

4.3. Momentum transmission coefficient T_{Jz}

In order to summarize the results obtained in the previous sections, we inspect the maximum of the transmission coefficient T_{Jz} in Figs. 6 and 10, as a function of the impurity potential and concentration, for three different values of mass, $m = 0, 0.05, 0.1$ (see Fig. 12). These data summarize the loss of momentum, hence resistivity, due to the random impurities, formally measured by:

$$\eta(C, V) = \max(T_{Jz}(C, V)). \quad (20)$$

From these figures, we observe that at high impurity concentration, $C = 0.05$ and a barrier $V = 100$ meV, the relativistic wave packet loses about 50% of its momentum, as compared with the case of a pure sample ($C = 0$). At the same concentration, a massive wave packet with $m = 0.1$, would lose more than 80%, indicating a significant drop of transmissivity due to inertia. At low impurity level, $C = 0.001$, both massless and massive wave packets show a mild reduction of transmittivity, below 10%.

Let us now define the following “transmittance”:

$$\Sigma(C, V) \equiv \frac{\eta}{1 - \eta}. \quad (21)$$

This definition allows one to draw a quantitative parallel with the concept of permeability of a classical fluid moving through a porous medium. That is, when the transmittance is unity, the conductivity goes formally to infinity, whereas zero transmittance connotes zero conductivity.

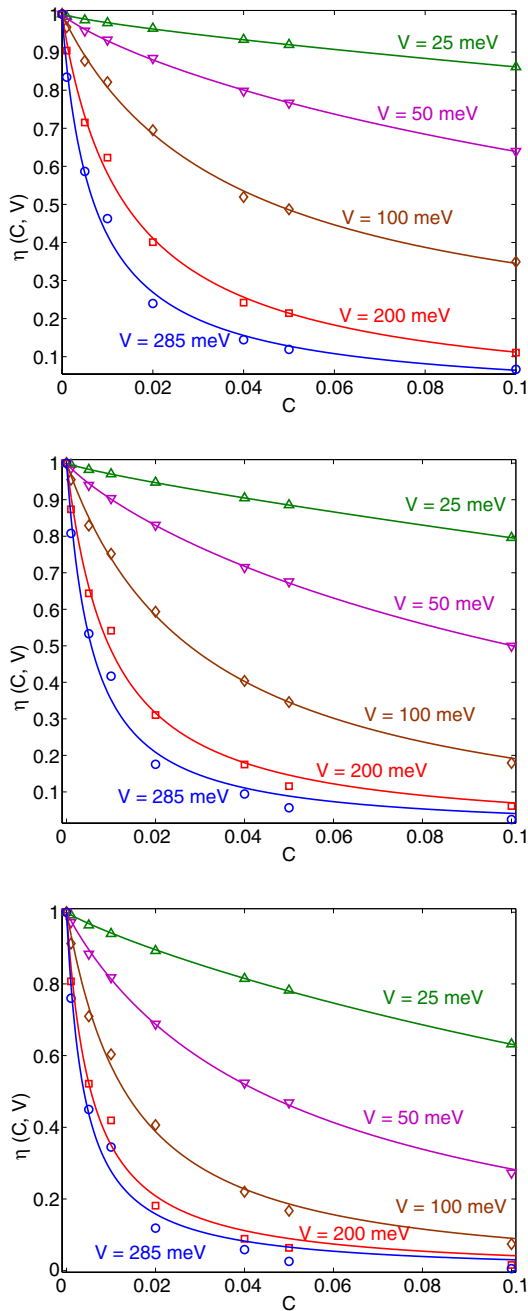


Fig. 12. (Color online) Maximum value of T_{Jz} as a function of the impurity percentage for each value of the impurity potential $V = 50-285$. For three values of the mass, $m = 0$ (top), 0.05 (middle), 0.1 (bottom).

Table 1. Set of parameters that has been obtained by fitting the numerical results for Σ using Eq. (21).

	V (meV)	25	50	100	200	285
$m = 0$	A	1.09	0.26	0.046	0.017	0.0097
	n	0.8	0.85	0.98	0.97	0.94
	Σ_0	0.51	0.23	0.17	0	0
$m = 0.05$	A	0.68	0.16	0.03	0.009	0.005
	n	0.84	0.88	0.99	1.01	1.01
	Σ_0	0	0	0	0	0
$m = 0.1$	A	0.27	0.053	0.011	0.0053	0.0039
	n	0.89	0.96	1.04	1.01	1.00
	Σ_0	0	0	0	0	0

Using Eqs. (20) and (21), we have found that the numerical results are satisfactorily fitted by the following analytical expression:

$$\Sigma(C, V) = A \frac{(1 - C)^{n+1}}{C^n} + \Sigma_0, \quad (22)$$

where A, n, Σ_0 are fitting parameters, which depend on the strength of the potential and the mass of the particles. In Fig. 12, we report the results of the fitting (solid line), showing good agreement with the numerical data. We have plotted η instead of Σ , in order to avoid the divergence at $C = 0$. The values of the parameters can be found in Table 1. From this table, we appreciate that the residual Σ_0 , is zero when the mass is different from zero, which points to this minimum permeability (conductivity) as to a property of massless particles. On the other hand, massive particles show a closer adherence to the Kozeny–Carman law, in the context of classical fluid-dynamics,^{4–8} where no residual conductivity is observed at $C = 1$. Also, note that for low potential barriers, the exponent is around $n \sim 0.85$, while for intermediate and strong potentials it is near $n \sim 1$, i.e. the value it takes for classical fluid-dynamics in a dilute disordered medium. Thus, for strong potentials, the classical analogy shows satisfactory results, while for intermediate and weak potentials, it presents deviations, typically of the order of 15%. Finally, we observe that the case $m = 0$ shows a significantly higher transmission than the corresponding data with $m > 0$, which is due to the higher momentum losses in the impurity region. It appears plausible to interpret the surplus of relativistic conductivity, especially for the three cases with energy $E < V$, as an indirect manifestation of Klein tunneling. Indeed, Klein tunneling requires $V > mc^2$, hence it becomes less effective with increasing mass. Differently rephrased, in the massive case the Dirac equation naturally reduces to the Schrödinger equation, which does not support any Klein tunneling.

5. Conclusions and Discussion

In this paper, we have performed a numerical study of a relativistic Gaussian wave packet propagating through a disordered medium, which we modeled as a set of randomly located potential barriers.

From the numerical results, we conclude that for high concentration of impurities, the wave packet presents higher losses in momentum. Furthermore, for a given impurity concentration, by increasing the potential of each impurity, we also find a loss of momentum. Systems with massive excitations are also studied. A nonzero mass is found to produce higher losses of momentum in the impurity region. The actual numerical values show that at high impurity concentration, $C = 0.05$, the wave packet loses more than half of its momentum with barriers of 100 meV and up to 85% with $V = 285$ meV. At low concentrations, $C = 0.001$, however, the losses are much milder, going from about 5–20%, for $V = 100$ –285 meV, respectively.

These data can be regrouped into an analytical expression, which bears a strong similarity with the permeability of porous media, as a function of the porosity. We have estimated the value of the conductivity from the transmission coefficient and fitted it by using the Carman–Kozeny law for porous media, relating the permeability with the concentration of impurities. We have found that this analogy works pretty well for the massive case, which shows no residual conductivity and a scaling exponent pretty close to unity. On the other hand, the massless case shows a residual conductivity. Moreover, for weak and intermediate potential strengths, the exponent is not unity, corresponding to a fractional Kozeny–Carman law. On the other hand, for strong potentials, the exponent one is recovered to a good accuracy, bringing the results closer to the analogy with classical fluids.³⁸ The applicability of this classical analogy indicates that, at least for the parameter set investigated in this paper, quantum tunneling is not the dominant transport mechanism, as compared to the semi-classical dynamics of the wave function, which can turn around the obstacles in a similar way as a classical fluid would do.

Finally, as a byproduct, we have introduced a new single-particle tool to model fermionic transport through disordered media, namely the QLB method. The present QLB solves the one-particle Dirac equation, but future extensions to include effective many-body interactions can also be conceived. QLB shares a remarkable computational efficiency, especially on parallel computers, and easy handling of complex geometries with its well-established classical LB counterpart. As a result, it is hoped and expected that the present model can make a contribution to the computational study of transport phenomena in any physical system governed by the Dirac equation.

Acknowledgments

The authors are grateful for the financial support of the Eidgenössische Technische Hochschule Zürich (ETHZ) under Grant No. 06 11-1.

References

1. O. Klein, *Z. Phys. A, Hadrons Nuclei* **53**, 157 (1929).
2. K. S. Novoselov *et al.*, *Nature* **438**, 197 (2005).
3. K. Novoselov *et al.*, *Science* **306**, 666 (2004).

4. R. R. Rumer and P. A. Drinker, *Proc. Amer. Soc. Civil Engrg., J. Hydraulic Div.* **92**, 155 (1966).
5. J. Bear, *Dynamics of Fluids in Porous Media* (American Elsevier Publishing Company, 1972).
6. J. Kozeny, *Sitzungsber Akad. Wiss.* **136**, 271 (1927).
7. P. C. Carman, *Trans. Inst. Chem. Engrg.* **15**, 150 (1937).
8. P. C. Carman, Flows of gases through porous media (Academic Press, 1956).
9. K. Nomura and A. H. MacDonald, *Phys. Rev. Lett.* **98**, 076602 (2007).
10. V. M. Galitski *et al.*, *Phys. Rev. B* **76**, 245405 (2007).
11. E. Rossi and S. Das Sarma, *Phys. Rev. Lett.* **101**, 166803 (2008).
12. M. Polini *et al.*, *Phys. Rev. B* **78**, 115426 (2008).
13. S. Das Sarma, S. Adam, E. H. Hwang and E. Rossi, *Rev. Mod. Phys.* **83**, 407 (2011).
14. A. F. Young and P. Kim, *Nat. Phys.* **5**, 222 (2009).
15. N. Stander, B. Huard and D. Goldhaber-Gordon, *Phys. Rev. Lett.* **102**, 026807 (2009).
16. V. V. Cheianov, V. Fal'ko and B. L. Altshuler, *Science* **315**, 1252 (2007).
17. C. W. J. Beenakker, R. A. Sepkhanov, A. R. Akhmerov and J. Tworzydlo, *Phys. Rev. Lett.* **102**, 146804 (2009).
18. S. Ghosh and M. Sharma, *J. Phys., Condens. Matter* **21**, 292204 (2009).
19. F. M. Zhang, Y. He and X. Chen, *Appl. Phys. Lett.* **94**, 212105 (2009).
20. J. M. Pereira, V. Mlinar, F. M. Peeters and P. Vasilopoulos, *Phys. Rev. B* **74**, 045424 (2006).
21. M. R. Setare and D. Jahani, *Physica B, Condens. Matter* **405**, 1433 (2010).
22. K. Y. Rakhimov, A. Chaves, G. A. Farias, F. M. Peeters, *J. Phys., Condens. Matter* **23**, 275801 (2011).
23. M. S. Jang, H. Kim, H. A. Atwater and W. A. Goddard, *Appl. Phys. Lett.* **97**, 043504 (2010).
24. S. Succi and R. Benzi, *Physica D* **69**, 327 (1993).
25. S. Palpacelli, S. Succi and R. Spigler, *Phys. Rev. E* **76**, 036712 (2007).
26. P. Dellar and D. Lapitski, *Phil. Trans. Roy. Soc. A* **369**, 2155 (2011).
27. P. J. Dellar, D. Lapitski, S. Palpacelli and S. Succi, *Phys. Rev. E* **83**, 046706 (2011).
28. S. Palpacelli and S. Succi, *Commun. Comput. Phys.* **4**, 980 (2008).
29. R. Benzi, S. Succi and M. Vergassola, *Phys. Rep.* **222**, 145 (1992).
30. V. B. Berestetskii, L. P. Pitaevskii and E. Lifshitz, *Quantum Electrodynamics*, 2nd edn. (Butterworths-Heinemann, Oxford, 1982).
31. J. Tworzydlo *et al.*, *Phys. Rev. B* **78**, 235438 (2008).
32. M. Bernaschi *et al.*, *Comput. Phys. Commun.* **180**, 1495 (2009).
33. M. Bernaschi *et al.*, *Proc. Int. Conf., High Performance Computing, Networking, Storage and Analysis (SC)*, November 12–18, 2011, Gordon Bell Award Honorable Mention.
34. M. I. Katsnelson, K. S. Novoselov and A. K. Geim, *Nat. Phys.* **2**, 620 (2006).
35. F. M. Peeters, *J. Phys., Condens. Matter* **23**, 275801 (2011).
36. J. M. Pereira Jr., F. M. Peeters, A. Chaves and G. A. Farias, *Semicond. Sci. Technol.* **25**, 033002 (2010).
37. G. Baym, *Lectures on Quantum Mechanics* (American Westview Press, 1990).
38. R. D'Agosta and M. Di Ventra, *J. Phys., Condens. Matter* **18**, 11059 (2006).
39. S. Succi, *Eur. Phys. J. B* **64**, 471 (2008).